

Natural Wax for Transient Electronics

Sang Min Won, Jahyun Koo, Kaitlyn E. Crawford, Aaron D. Mickle, Yeguang Xue, Seunghwan Min, Lisa A. McIlvried, Ying Yan, Sung Bong Kim, Seung Min Lee, Bong Hoon Kim, Hokyoung Jang, Matthew R. MacEwan, Yonggang Huang, Robert W. Gereau IV, and John A. Rogers*

Emerging classes of bioresorbable electronic materials serve as the basis for active biomedical implants that are capable of providing sensing, monitoring, stimulating, and other forms of function over an operating period matched to biological processes such as wound healing. These platforms are of interest because subsequent dissolution, enzymatic degradation, and/or bioresorption can eliminate the need for surgical extraction. This report introduces natural wax materials as long-lived, hydrophobic encapsulation layers for such systems, where biodegradation eventually occurs by chain scission. Studies of wax stability as an encapsulation material demonstrate the ability to retain operation of underlying biodegradable electronic systems for durations between a few days to a few weeks during complete immersion in aqueous solutions in ex-vivo physiological conditions. Electrically conductive composites result from the addition of tungsten micro/nanoparticles, as a conductive, printable paste with similar lifetimes. Demonstrations of these materials in partially biodegradable wireless light-emitting diodes and near-field communication circuits illustrate their use in functional bioresorbable electronic systems. Investigations in animal models reveal no signs of toxicity or other adverse biological responses.

materials that can degrade in a benign, controlled fashion when immersed in ground water and biofluids. The vision is for electronic devices that can naturally degrade into the environment to eliminate costs and hazards associated with discarded devices, and for active implants that can bioresorb into the body to avoid the risks associated with surgical extraction procedures. The need for the former is increasingly urgent due to increase in the proliferation of electronic goods and decrease in the cycle times for introduction of new technology generations.^[1–6] The opportunities for the latter are equally significant, where biodegradable electronic systems have the potential to treat disease and wound healing in ways that can complement traditional pharmacological approaches.^[7–11]

Both areas rely on the development of active and passive materials that support high-performance electronic functionality and degrade in aqueous environments

to benign end products. Recent research highlights a range of transient options in semiconductors,^[12–16] metals,^[17–19] and thin film dielectrics.^[19–21] A remaining challenge is the development of encapsulating materials for applications that demand stable operation for timescales ranging from a few days to

1. Introduction

Challenges in management of waste streams associated with consumer electronic devices and opportunities in temporary biomedical implants motivate research into classes of electronic

S. M. Won, S. Min, S. M. Lee, H. Jang
Department of Electrical and Computer Engineering
Frederick Seitz Materials Research Laboratory
University of Illinois at Urbana-Champaign
Urbana, IL 61801, USA

Dr. J. Koo, Dr. S. B. Kim, Dr. B. H. Kim
Department of Materials Science and Engineering
Northwestern University
Evanston, IL 60208, USA

Prof. K. E. Crawford
Department of Materials Science and Engineering
University of Central Florida
Orlando, FL 32816, USA

Dr. A. D. Mickle, Dr. L. A. McIlvried, Prof. R. W. Gereau IV
Department of Anesthesiology
Washington University Pain Center
Washington University School of Medicine
St. Louis, MO 63130, USA

DOI: 10.1002/adfm.201801819

Y. Xue, Prof. Y. Huang
Department of Mechanical Engineering
Department of Civil and Environmental Engineering
Department of Materials Science and Engineering
Northwestern University
Evanston, IL 60208, USA

Dr. Y. Yan, Prof. M. R. MacEwan
Department of Neurological Surgery
Washington University School of Medicine
St Louis, MO 63110, USA

Prof. J. A. Rogers
Center for Bio-Integrated Electronics
Department of Materials Science and Engineering
Biomedical Engineering, Chemistry, Mechanical Engineering
Electrical Engineering and Computer Science, and Neurological Surgery
Simpson Querrey Institute for Nano/biotechnology
McCormick School of Engineering and Feinberg School of Medicine
Northwestern University
Evanston, IL 60208, USA
E-mail: jrogers@northwestern.edu

a few weeks. Deposited inorganic coatings provide some useful capabilities in this context, but their mechanical fragility and their typically unacceptably high density of defects limit their utility. Polymer thin films represent additional options, but their water permeability and tendency to swell upon exposure to water are unfortunate disadvantages. For example, layers of common biodegradable polymers such as poly(lactic-co-glycolic acid) (PLGA) and silk fibroin are permeable to water, and they often exhibit swelling due to water uptake, which can lead to delamination from the device; hence, materials such as polylactic acid (PLA), PLGA, silk etc., are non-ideal encapsulants for electronic materials (Figure S1, Supporting Information).^[22]

This paper evaluates the potential of soy, myrtle, and candelilla wax materials derived from soybeans (via soybean oil), myrica cerifera (myrtle), and candelilla shrubs, respectively, to be used as encapsulation layers in bio/eco resorbable electronics. These natural wax materials are of interest compared to their petroleum-derived counterparts because they are largely environmentally and biologically degradable.^[23–27] Their composition involve complex mixtures of compounds that include, but are not limited to, long-chain poly- and mono-unsaturated esters, fatty acids, and anhydrides, along with short-chain hydrocarbons (ca. 29–33 carbons/chain) and resins, such as triterpenes.^[26–29] The ratios of these compounds vary depending on the source of the wax, resulting in a series of natural materials with unique properties. For example, in consideration of the water vapor transmission rate (WVTR) of these wax materials, the rate is likely to decrease with increasing hydrophobic hydrocarbon content, while the rate of biodegradation (and WVTR) of the same materials will likely to occur more readily with a greater incorporation of reactive functional groups such as esters, anhydrides, and sites of unsaturation when exposed to the same experimental conditions. The results in the following explore the key considerations and present examples of applications as biodegradable encapsulants and as matrices for composite conductors that incorporate micro/nanoparticles of tungsten. In all cases, the hydrophobic character of the wax and the presence of biodegradable functional groups are essential features of the materials.

2. Results and Discussion

Encapsulation layer: Analysis by gas chromatography coupled with mass spectroscopy (GC-MS) reveals that candelilla wax has the highest hydrocarbon content of the three waxes explored here. The results for candelilla wax are in **Figure 1A**. The red peaks represent saturated hydrocarbons (intact or as fragment from higher order structures such as fatty acids), the blue peaks represent ester, anhydride or free-acid derivatives, and the green peaks correspond to compounds of higher complexity such as mono- or poly-unsaturated chains, lupeol, and other unidentified resin-like compounds. The anhydrides and anhydride derivatives are likely fragments of fatty-acid structures known to be present in most natural wax compositions.^[26–30] The GC data for myrtle wax is in the Supporting Information (Figure S2) and composition of soy wax can be found elsewhere.^[31] In comparing wax compositions based on GC-MS and literature,

the results indicate that soy wax possesses the least amount of hydrocarbon (*vis.* candelilla > myrtle > soy in relative hydrocarbon content). Each wax has a hydrophobic character (water contact angle measurement > 90° for each wax type, Figure S3, Supporting Information), but the degree of water uptake and moisture permeability differ, as defined by measurements of the change in water absorption (deionized, DI) per sample area (mg cm⁻²) with time (up to 15 d). The results reveal similar water uptake behavior at room temperature (RT, 24 °C, Figure S4, Supporting Information), but different behavior at physiological temperature (37 °C, Figure 1B). For the latter, the candelilla wax exhibits almost no water uptake over 15 d (Figure 1B; blue dots), myrtle wax absorbs water steadily up to ≈12 mg cm⁻² at 15 d (Figure 1B; green dots), and soy wax absorbs more than 24 mg cm⁻² after only 2 d (Figure 1B; red dots). Here, water absorption test parameters follow from standards defined by the American Society for Testing and Materials, as described in the Experimental Section, where the weights of circular samples (thickness of 10 mm and diameter of 40 mm) immersed in DI water at 37 °C are measured as a function of time.

Additional information follows from studies of time dependent fractional changes in the resistance ($\Delta R/R_0\%$ versus time in days) of serpentine traces of Mg (length 43 mm, width 300 μm, and thickness 200 nm) encapsulated with films of wax (thickness 300 μm) during immersion in phosphate buffer solution (PBS; pH 7.4, 0.01 × 10⁻³ M) at 37 °C. Here, increases in resistance correspond to hydrolysis of the Mg [Mg + 2H₂O → Mg(OH)₂ + H₂] due to diffusion of moisture through the wax. Encapsulation with candelilla wax yields unchanging resistances over 7 d, with rapid increases that begin to occur from the 10th day until complete electrical disconnection by day 15. Soy and myrtle wax, both exhibit large changes in resistance, which occur shortly after immersion ($\Delta R/R_0 \geq 300\%$ in < 1 d), as shown in Figure 1C. The combined results (water uptake and changes in resistance) suggest that candelilla wax is the most promising of the three candidate materials for encapsulation and thus is the focus of the remaining studies described in the following.

The effectiveness of any encapsulation depends on the thickness, as summarized by studies of candelilla wax at three different thicknesses using the same Mg test structure described above. The average times to reach fractional resistance changes of 100% are 4, 7, and 11 d for films with thicknesses of 100, 200, and 300 μm, respectively, as in Figure 1D. Here, a 1D analytical model, detailed in the Experimental Section, allows study of the reactive diffusion of water through the wax encapsulation. The diffusivity estimated in this manner is $D_{\text{wax}} = 6.05 \times 10^{-15} \text{ m}^2\text{s}^{-1}$, which is close to the lower bound of reported diffusivity for apple wax.^[32] Images of a Mg film (surface area 1 cm² and thickness: 200 nm) encapsulated with a 300 μm thick layer of candelilla wax during immersion in PBS (pH 7.4) at 37 °C captured as a function of time are reproduced in Figure 1E. Consistent with tests of device stability in Figure 1C,D, dissolution of Mg occurs after a stable period of up to 6 d with no sign of water penetration. On day 7, effects of hydrolysis become visually apparent until the film completely disappears by day 13. Images at both days 7 and 13 show that the dissolution of Mg occurs across the entire area of the film,

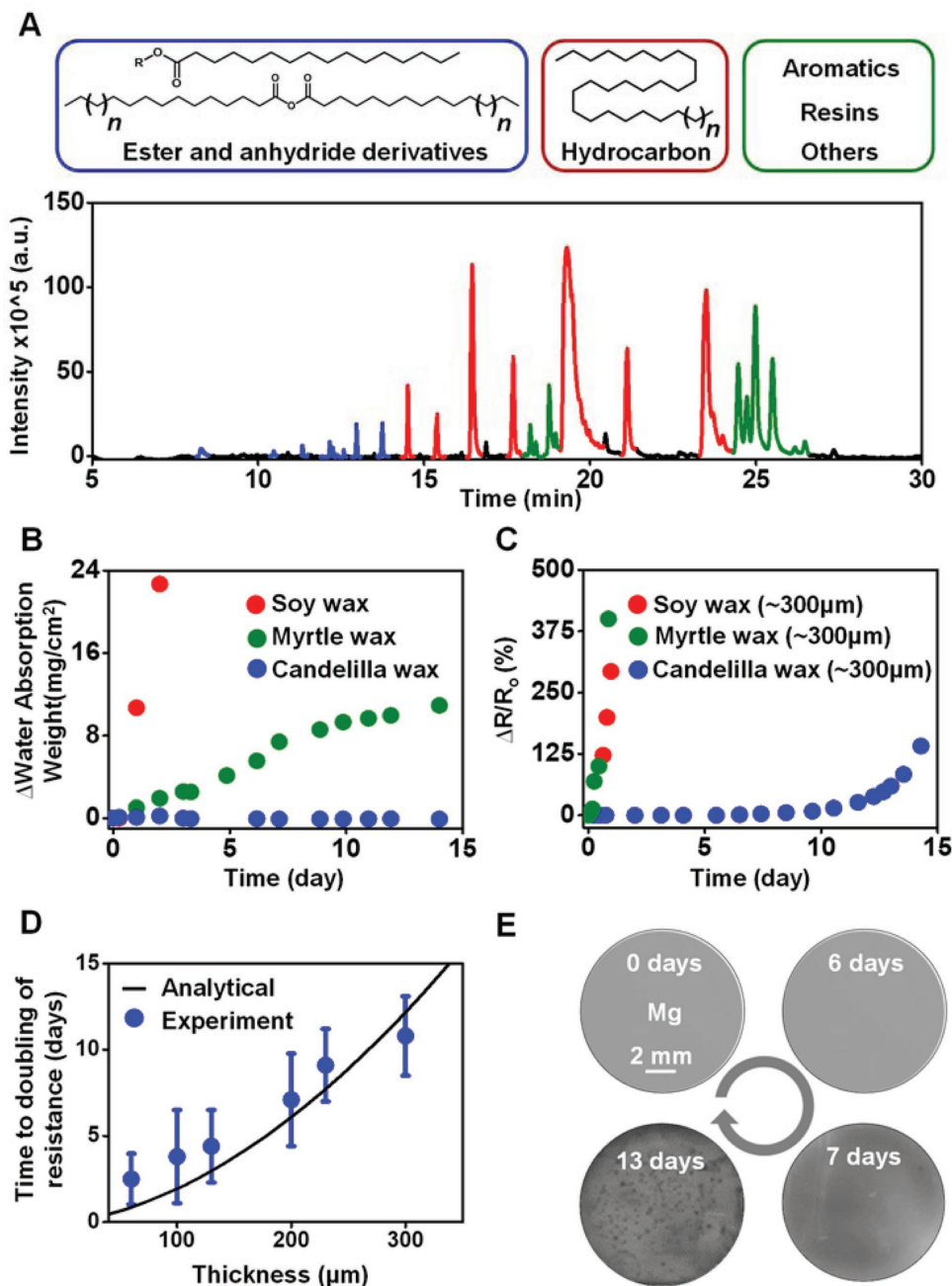


Figure 1. Chemical composition and water permeability of plant-based wax materials. A) GC-MS analysis of candelilla wax reveals a range of hydrocarbon chain lengths (where n is $\approx \geq 1$ and ≤ 15). A summation of peak areas indicate a primary composition of hydrocarbons with esters, anhydrides, acid derivatives, and fatty acids, with aromatic compounds present at a lower concentration. The molecular assignments correspond to direct comparisons with the NIST library. B) The water absorption behavior of candelilla, myrtle, and soy wax was measured in DI water at 37 °C. C) Relative water permeation properties of candelilla, myrtle, and soy wax encapsulation layers were determined by the time dependence of the resistance of a thin film trace of Mg. Water that penetrates through the encapsulation layers dissolves the Mg, thereby increasing the resistance. D) Time for the resistance of Mg film to double as function of the wax encapsulation thickness. E) Time sequence of images of Mg encapsulated by candelilla wax (thickness of 300 μ m) immersed in PBS solution at 37 °C.

consistent with spatially homogeneous water/moisture transport through the wax encapsulation layer.

Biodegradability is also a key factor in considering materials for use in bioresorbable electronics. Based on the chemical make-up of candelilla wax reported in the literature^[26] and reported here, dissolution of candelilla wax likely occurs by

cleavage of the ester, anhydride, and like moieties via hydrolysis (Figure S5, Supporting Information). The degradation process can be characterized by measuring the thickness of a film of material (1.0 cm \times 1.0 cm \times 800 μ m) after three months of implantation within the subdermal dorsal (back) region of four separate rats. After extraction at three months, candelilla

wax sample thickness decreased by $28 \pm 4 \mu\text{m}$ (Figure S6, Supporting Information), which is comparable to that reported for different natural bees wax materials in similar studies.^[33] The continuous decrease in weight associated with a sample of wax in PBS at pH 7.4 at 48°C (temperature higher than physiological used to expedite degradation) is also consistent with dissolution that involves very little water absorption and/or swelling (Figure S7, Supporting Information).

Biodegradable conductive paste: These wax materials can also be used as biodegradable matrices for conductive pastes, of use for non-planar interconnects, low resistance antennas, and other features that require thick film conductors. Candelilla wax, loaded with tungsten microparticles (particle diameter of $\approx 5 \mu\text{m}$, Figure S8, Supporting Information) using

a straightforward mixing process described in the Experimental Section, yields a conductive wax (C-wax) with attractive transient electronic characteristics. Figure 2A shows a scanning electron microscope (SEM) image of a representative C-wax formulation (left); the image on the right includes a color rendering of chemical composition determined by energy dispersive x-ray spectroscopy, where pink and green regions correspond to tungsten and wax, respectively.

Figure 2B summarizes measurements of the direct current (DC) conductivity of C-wax as a function of volume fraction of W microparticles. The conductivity, σ , of such a binary composite can be modeled as

$$\sigma = \sigma_0 (\phi - \phi_c)^t \text{ for } \phi > \phi_c \quad (1)$$

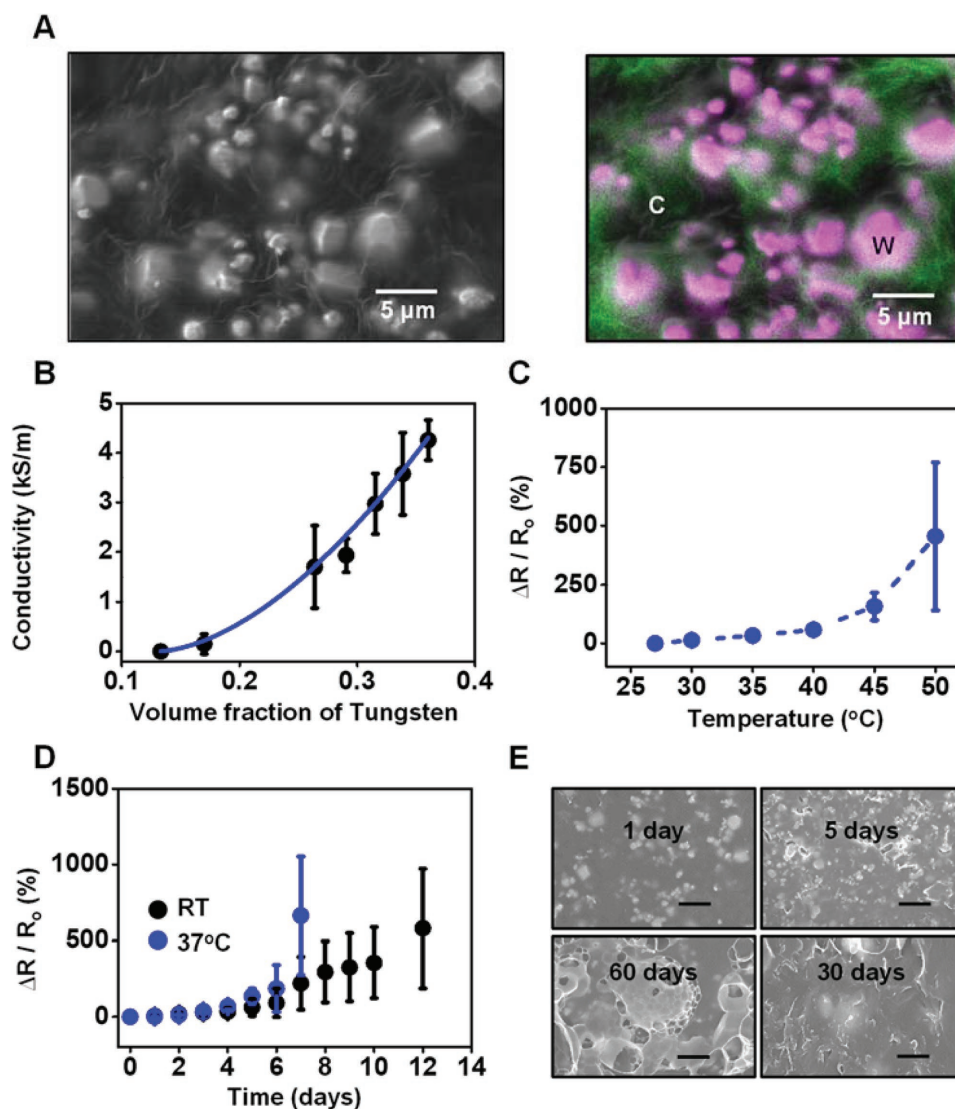


Figure 2. Characteristics of electrically conductive composites of wax and microparticles of tungsten. A) SEM images of candelilla wax mixed with tungsten microparticles (left; C-wax). The corresponding energy dispersive spectroscopy image (right) indicates regions of high carbon (green) and tungsten (pink) content. B) DC conductivity of C-wax as a function of volume fraction of tungsten. C) Fractional change in resistance ($\Delta R/R_0$) of a patterned feature of C-wax (2 mm width, 20 mm length, and $100 \mu\text{m}$ thickness) with temperature from RT to 50°C . D) Fractional change in resistance ($\Delta R/R_0$) of a patterned feature of C-wax (2 mm width, 20 mm length, and $100 \mu\text{m}$ thickness) as a function of time of immersion in PBS solution at RT (black dots) and 37°C (blue dots). E) Series of images showing processes of dissolution of C-wax during immersion in DI water at 50°C . (Scale bar: $8 \mu\text{m}$).

where σ_0 is a scaling factor, ϕ is the volume fraction, ϕ_c is the critical volume fraction (percolation threshold), and t is a critical exponent that defines the dimensionality of the network.^[34,35] Fitting the measured data to this model yields $\phi_c \approx 0.13$ (weight fraction: ≈ 0.75) and $t \approx 1.6$, comparable to values for related systems.^[36]

Figure 2C shows the fractional change in resistance ($\Delta R/R_0$) of C-wax as function of temperature. The results are consistent with non-resorbable wax composites (carbon fiber in paraffin wax), where the volume expansion of the wax at temperatures below the melting point increases the tunneling barrier and decreases the contact area between particles for conduction.^[37,38] The $\Delta R/R_0$ remains below a 100% change up to 45 °C, suggesting relatively stable electrical properties at physiological temperatures (37 °C). Figure 2D shows $\Delta R/R_0$ of C-wax with a tungsten volume fraction of 0.35 as a function of time of immersion in PBS at 37 °C and RT. $\Delta R/R_0$ remains below a 100% change for ≈ 5 d at 37 °C, qualitatively consistent with studies using the Mg test structure described previously. Figure 2E shows SEM images of C-wax at several stages of dissolution in DI water at 50 °C. Here, cracks appear after 5 d and further fragmentation occurs afterward, indicating the water penetration through the tungsten particles and wax matrix, and consequent dissolution of particles cause the rate of resistance change in Figure 2D.

Biodegradable electronics: Figure 3 summarizes demonstrations of candelilla wax as encapsulants and conductive composites (with tungsten volume fraction of 0.35). Figure 3A shows an image of radio frequency (RF) inductive coil ($\approx 50\text{-}\mu\text{m}$ -thick magnesium foil) on a biodegradable substrate, PLGA, designed to provide wireless power to a light-emitting diode (LED) electrically connected to the coil using C-wax applied by melting (75 °C) and then drop casting at RT. Encapsulating such electronics in candelilla wax using a similar melting and casting process results in fully biodegradable systems capable of operation in PBS at RT for over 15 d as shown in Figure 3B. Figure 3C presents a near-field communication (NFC) device based on replacing the LED with an NFC chip (Texas Instruments, TRF7970A). This device enables wireless, reading and writing of data onto the chip. This working device also shows the no cracks or signs of wear after at least 3 d of implantation in the abdomen of a rat model (Figure S9, Supporting Information).

In these and other applications, the patterning method of the C-wax is important. Figure 3D presents a trace of C-wax formed by direct writing with a heated (≈ 90 °C) metal tip that melts and transfers the C-wax, as a conductive ink, on a target substrate. Connecting the system to a 3.0 V power supply activates the LED, thereby demonstrating the electrical conductivity of the traces and their interface to the LED. The ease of molding, printing, and casting the wax using poly(dimethylsiloxane) (PDMS) molds serves as the basis for additional options in patterning. As an example, a combination of non-conductive and conductive wax-based bricks (white: soy wax, yellow: candelilla wax, and black: C-wax), similar to LEGO, enables a 3D circuit (Figure 3E). Here, simple assembly of conductive pathways and integration with non-conductive bricks, yields an architectural arrangement that does not require any wires for this circuit demonstration. Patterning C-wax by screen printing can also form complex shapes such as a circular RF antenna (line width ≈ 0.7 mm of and outer diameter of ≈ 53 mm) as shown in

Figures 3F,G. The process begins by preparing a PDMS mold by the techniques of soft lithography, followed by casting a molten C-wax composite to fill the recessed regions, as shown in top frame of Figure 3F. Drop casting of candelilla wax on top forms a coating that mechanically joins the features of C-wax to yield a final structure that can be physically removed from the mold providing wax-based pieces for use in electronics. This screen printing process can generate C-wax in various small feature sizes as shown in Figure S10 in the Supporting Information, where LEDs placed between two adjacent lines (feature size from 100 μm to 1 mm) serve as indicators of electrical conductivity. Figure 3G shows an example that integrates LEDs with a fully wax-based inductive coil and substrate for wireless power.

For interfaces with soft tissues of the body, the mechanical properties can be important. Figure S11 in the Supporting Information shows the Shore-D hardness for various known non-biodegradable encapsulants compared to the wax materials evaluated in this study, and the maximum degree of bending for five different candelilla wax thicknesses. The results suggest that the hardness of the wax materials is comparable to those of established encapsulants (i.e., epoxy, stainless steel, and glass). Wax samples with thicknesses lower than 200 μm are bendable to radii of 20 mm, but cracks tend to form at thicknesses larger than 300 μm at the same 20 mm radii. Studies to improve the mechanical properties without hindering the barrier properties are currently underway.

In vivo biocompatibility: Biocompatibility of both candelilla and C-wax are important for applications in both consumer electronic devices and biomedical implants. Previous studies have demonstrated the biocompatibility of tungsten and natural wax individually.^[27,39–41] To further examine biocompatibility of these materials together, we implanted candelilla and C-wax (1 cm \times 1 cm \times 800 μm) subcutaneously in the abdominal region of mice and examined overall health and immune reaction in adjacent skin. Skin tissue sections stained with hematoxylin and eosin (H&E) show no changes in gross histology and immune cell infiltration compared to sham surgery skin (Figure 4A). To further quantify the immune reaction to these implanted materials, skin sections were stained with the antibody CD45, a pan-immune cell marker. There were no significant differences in overall intensity of CD45 staining between candelilla, C-wax, and sham surgery groups (Figure 4B,C). There were also no significant differences in weight gain between candelilla, C-wax, and sham groups of mice, suggesting that both wax materials have no observable effect on the overall animal health and normal growth (Figure 4D). These results confirm and support the previous biocompatibility studies, demonstrating both candelilla and C-wax are biocompatible and do not initiate significant immune responses.

3. Conclusion

The results of these studies provide examples of wax-based materials that can be tailored for use as encapsulation layers, substrates, and conductive composites for biodegradable electronics that can operate in a stable fashion over extended periods of time in aqueous environments. Fundamental chemical and electrical studies reveal key properties such as water permeability, biodegradability, conductivity, and stability.

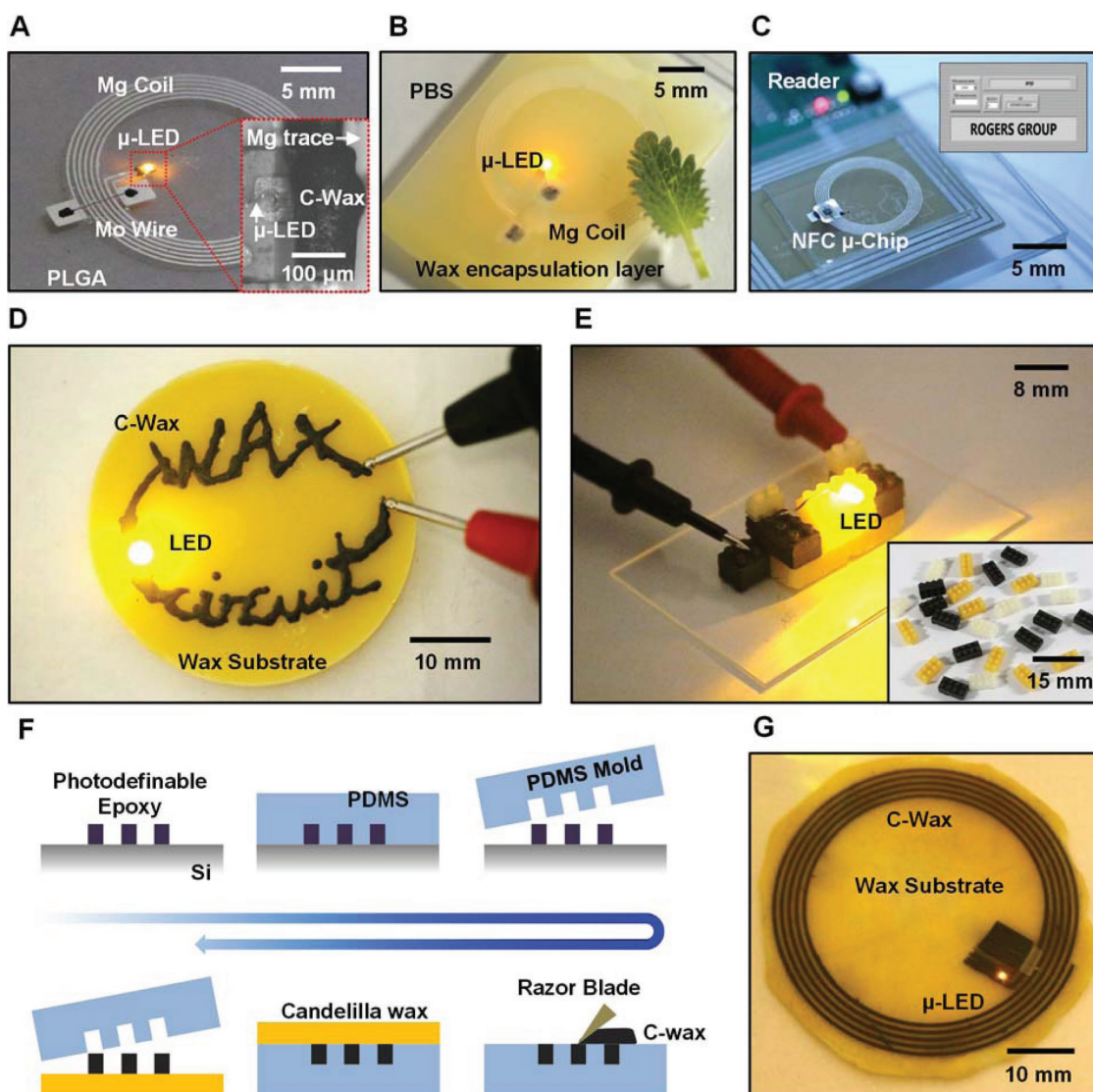


Figure 3. Integration of insulating and C-wax formulations into biodegradable electronic devices. A) Wireless device that uses C-wax for electrical interconnection of various circuit components (Mo wire, LED, and capacitors) and an RF coil of Mg. B) Operation of such a device encapsulated in layer of candelilla wax (300 μm) on top and bottom, in PBS solution at RT for 15 d. The leaf was added to further visualize the depth of PBS solution. C) Demonstration of wireless readout of data stored in an NFC chip. D) Electrically conductive trace formed by direct writing of C-wax with a heated metal tip. E) Demonstration of electrical connection through an assembly of C-wax based bricks. The inset shows various wax-based bricks, similar to LEGO. Yellow, white, and black bricks correspond to candelilla, soy, and C-wax composite, respectively. F) Illustration of the screen printing process used to form a C-wax-based RF inductive coil on a candelilla wax substrate. G) Demonstration of wireless power delivery through the C-wax-based RF inductive coil. Here, an Mo wire electrically joins the start and end points of the coil to close the loop.

Demonstrations in partially biodegradable wireless LED and NFC circuits illustrate the functional use of these materials. The ease of processing, enabled by the low melting points of these materials, further supports various routes for patterning and integration. In vivo studies suggest that these materials and their dissolution products are biocompatible.

4. Experimental Section

Gas Chromatography Mass Spectroscopy: Chemical analysis of wax samples involved a Waters GCI Premier GC-MS operated in high-resolution mode with electron-ionization (EI) and splitless injection

(1 μL injection volume). The carrier gas (Helium) was maintained at a rate of 50 L min^{-1} , with a temperature ramp of 10 $^{\circ}\text{C min}^{-1}$ for 30 min. Samples were prepared with concentrations of 1–2 mg mL^{-1} in chloroform and were filtered through a 0.2 μm PTFE filter.

Tests of Water Uptake: Melting and casting wax (melting points are in Figure S12, Supporting Information) samples in a PDMS mold yielded cylinders with diameters and thicknesses of 4 and 1 cm, respectively (Figure S13, Supporting Information). The initial weights were 13.72, 14.50, and 13.96 g for Soy (Akosoy Natural Soy 125 (415) Wax, Mels Candles, Rolla MO USA), Myrtle (Milliard Premium Vegan Bayberry Wax), and candelilla Wax (Sigma-Aldrich), respectively. Immersing the samples in DI water at 37 $^{\circ}\text{C}$, removing the samples from the solution, and weighing them at several different times yielded the weight of absorbed water.

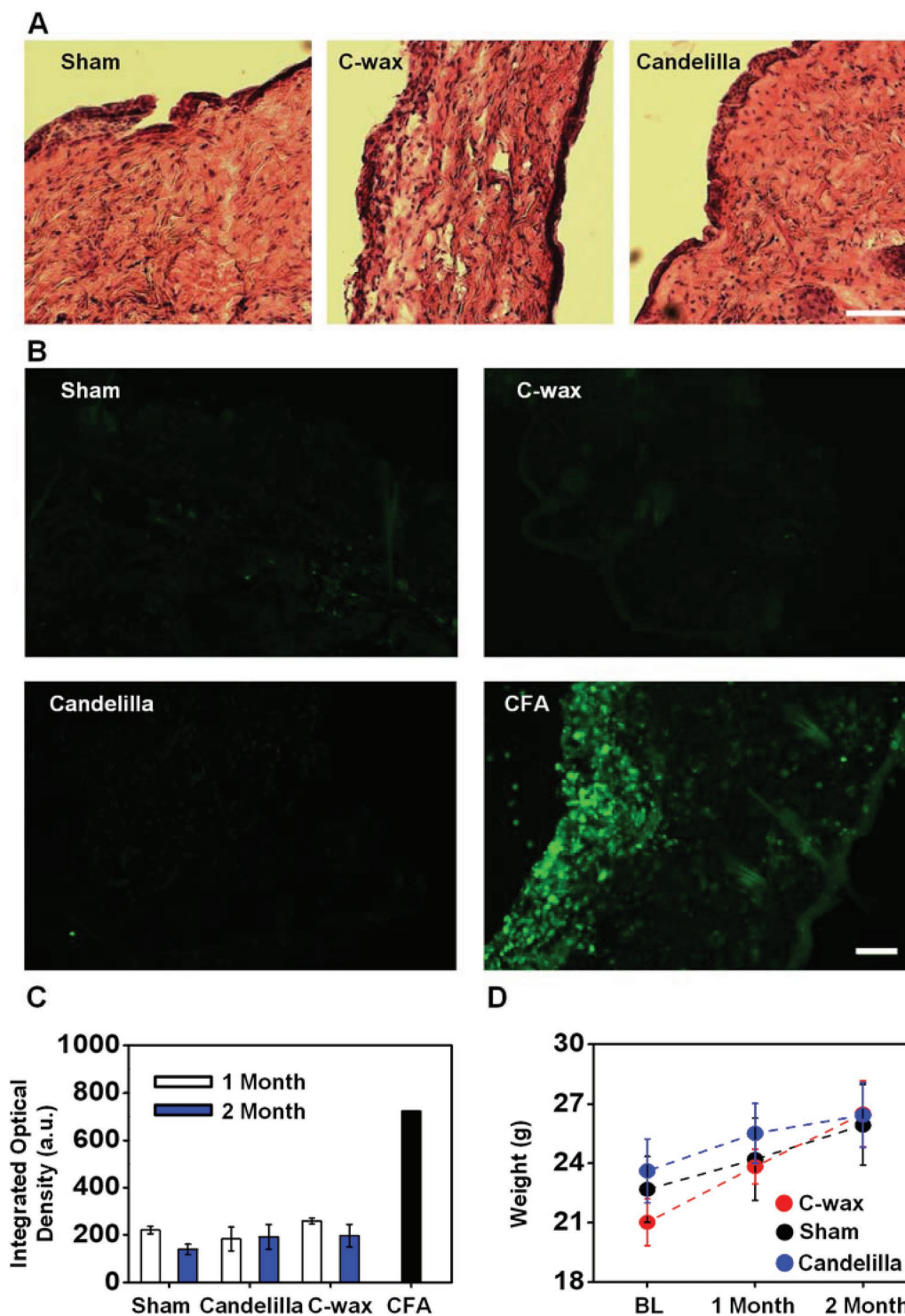


Figure 4. Biocompatibility of wax formulations. A) Representative images of H&E stained skin from mice implanted with candelilla, C-wax or sham surgery. (scale bar 200 μ M). B) Representative images of CD45 staining in skin from mice two months following implantation of Candelilla, C-wax, sham surgery, or 24 h following injection of CFA as a positive control for inflammation (scale bar 200 $\times 10^{-6}$ μ m). C) Quantification of CD45 staining intensity, demonstrating no significant differences between the sham, Candelilla and C-wax groups ($n = 2-3$ animals per group). (Two-way ANOVA, 1 Month Sham versus Candelilla $P = 0.7740$, 1 Month Sham versus Conductive Wax $P = 0.8041$, 2 Month Sham versus Candelilla $P = 0.6081$, and 2 Month Sham versus Conductive Wax $P = 0.5567$). D) Mouse weights before, one and two months after implantation of Candelilla, C-wax or sham surgery (BL = baseline; $n = 6$ for BL and one month timepoint groups, $n = 3$ for two month timepoint groups). No significant differences were observed between the Candelilla, C-wax and sham surgery animals. (Two-way ANOVA, 1 Month Sham versus Candelilla $P = 0.3813$, 1 Month Sham versus Conductive Wax $P = 0.963$, 2 Month Sham versus Candelilla $P = 0.9313$, and 2 Month Sham versus Conductive Wax $P = 0.9127$). All data mean \pm standard deviation.

Tests of Water Permeation: Photolithography and lift-off using negative photoresist (AZ nLOF2070, MicroChemicals) yielded patterns of Ti/Mg (5 nm/200 nm) on a glass slide. A layer of Cr/Au (5 nm/150 nm) patterned in the same manner defined pads for electrical probing. Dip coating in a molten wax and bonding a well structure of PDMS (Sylgard 184, Dow Corning, USA) on top yielded a platform for testing water permeation (Figure S14, Supporting Information). The resistance values were averaged from seven different samples for each case.

Modeling of Reactive Diffusion for Wax Encapsulated Mg: The processes of diffusion and reaction of wax encapsulation on top of Mg while submerged in water (or PBS solution) can be described with models of reactive diffusion. A 1D analytical model can be used because the thickness of the wax/Mg sample ($h_0 + h_{\text{wax}}$, where h_0 and h_{wax} are the initial thicknesses of the Mg film and wax encapsulation, respectively, as shown in Figure S15, Supporting Information) is much smaller than its diameter. The reactive diffusion equations are given as

$$\begin{cases} D \frac{\partial^2 w}{\partial y^2} - kw = \frac{\partial w}{\partial t}, 0 \leq y \leq h_0 \\ D_{\text{wax}} \frac{\partial^2 w}{\partial y^2} = \frac{\partial w}{\partial t}, h_0 \leq y \leq h_0 + h_{\text{wax}} \end{cases} \quad (2)$$

where w is the water concentration as a function of time t and position y , D and k are the diffusivity of water and reaction constant in Mg, respectively, and D_{wax} is diffusivity of water in wax. Because waxes react with water slowly, the equation for $h_0 \leq y \leq h_0 + h_{\text{wax}}$ does not include the reaction term and degenerates to the standard diffusion equation. Water concentration is constant w_0 at the interface between water and top surface of wax and the water flux at the bottom surface of Mg is zero, i.e.,

$$w|_{y=h_0+h_{\text{wax}}} = w_0 \quad (3)$$

$$\frac{\partial w}{\partial y} \Big|_{y=0} = 0 \quad (4)$$

The initial condition is zero water concentration, i.e.,

$$w|_{t=0} = 0 \quad (5)$$

The continuity of concentration and flux of water molecules across the wax/Mg interface gives

$$w|_{y=h_0-0} = w|_{y=h_0+0} \quad (6)$$

$$D \frac{\partial w}{\partial y} \Big|_{y=h_0-0} = D_{\text{wax}} \frac{\partial w}{\partial y} \Big|_{y=h_0+0} \quad (7)$$

The solution of above equation is obtained, following the same method as Li et al.^[42] as

$$w(t, y) = w_0 \left[\sum_{n=1}^{\infty} C_n e^{-\lambda_n t} f_n(y) + g(y) \right] \quad (8)$$

where λ_n are eigenvalues determined from

$$\cos\left(\sqrt{\frac{\lambda-k}{D}} h_0\right) \cos\left(\sqrt{\frac{\lambda}{D_{\text{wax}}}} h_{\text{wax}}\right) = \sqrt{\frac{D(\lambda-k)}{D_{\text{wax}} \lambda}} \sin\left(\sqrt{\frac{\lambda-k}{D}} h_0\right) \sin\left(\sqrt{\frac{\lambda}{D_{\text{wax}}}} h_{\text{wax}}\right) \quad (9)$$

$g(y)$ and $f_n(y)$ are given as

$$g(y) = \begin{cases} \frac{1}{\sqrt{\frac{Dkh_{\text{wax}}^2}{D_{\text{wax}}} \sinh\sqrt{\frac{kh_0^2}{D}} + \cosh\sqrt{\frac{kh_0^2}{D}}} \cosh\left(\sqrt{\frac{k}{D}} y\right), 0 \leq y < h_0 \\ 1 - \frac{1}{1 + \sqrt{\frac{D_{\text{wax}}}{Dkh_{\text{wax}}}} \coth\left(\sqrt{\frac{kh_0^2}{D}}\right)} \frac{h_0 + h_{\text{wax}} - y}{h_{\text{wax}}}, h_0 \leq y < h_0 + h_{\text{wax}} \end{cases} \quad (10)$$

$$f_n(y) = \begin{cases} \sin\left(\sqrt{\frac{\lambda_n}{D_{\text{wax}}}} h_{\text{wax}}\right) \cos\left(\sqrt{\frac{\lambda_n - k}{D}} y\right), 0 \leq y < h_0 \\ \cos\left(\sqrt{\frac{\lambda_n - k}{D}} h_0\right) \sin\left[\sqrt{\frac{\lambda_n}{D_{\text{wax}}}} (h_0 + h_{\text{wax}} - y)\right], h_0 \leq y < h_0 + h_{\text{wax}} \end{cases} \quad (11)$$

and C_n are coefficients determined by initial condition as

$$C_n = \frac{-\frac{2}{\lambda_n} \sqrt{\lambda_n D_{\text{wax}}} \cos\left(\sqrt{\frac{\lambda_n - k}{D}} h_0\right)}{h_0 \sin^2\left(\sqrt{\frac{\lambda_n}{D_{\text{wax}}}} h_{\text{wax}}\right) \left[1 + \frac{\sin\left(2\sqrt{\frac{\lambda_n - k}{D}} h_0\right)}{2\sqrt{\frac{\lambda_n - k}{D}} h_0}\right] + h_{\text{wax}} \cos^2\left(\sqrt{\frac{\lambda_n - k}{D}} h_0\right) \left[1 - \frac{\sin\left(2\sqrt{\frac{\lambda_n}{D_{\text{wax}}}} h_{\text{wax}}\right)}{2\sqrt{\frac{\lambda_n}{D_{\text{wax}}}} h_{\text{wax}}}\right]} \quad (12)$$

The mass of water that reacts at a given location (per unit volume) is given by kw . The mass of dissolved Mg (per unit volume) is $kwM_{\text{Mg}}/(qM_{\text{H}_2\text{O}})$, where M_{Mg} and $M_{\text{H}_2\text{O}}$ are molar mass of Mg and water, respectively, and $q = 2$, which represents that two water molecules react with each Mg atom. The decrease of the volume of the Mg film is then obtained by integrating $kwM_{\text{Mg}}/(q\rho_{\text{Mg}}M_{\text{H}_2\text{O}})$ over both the thickness direction y and time t , where ρ_{Mg} is the density of Mg. The Mg thickness h normalized by its initial thickness h_0 is then given as

$$\frac{h(t)}{h_0} = 1 - \frac{w_0 M_{\text{Mg}}}{q \rho_{\text{Mg}} M_{\text{H}_2\text{O}}} k \left[\frac{1}{\sqrt{\frac{Dkh_{\text{wax}}^2}{D_{\text{wax}}} \sinh\sqrt{\frac{kh_0^2}{D}} + \cosh\sqrt{\frac{kh_0^2}{D}}} \frac{\sinh\sqrt{\frac{kh_0^2}{D}}}{\sqrt{\frac{kh_0^2}{D}}} + \sum_{n=1}^{\infty} \frac{C_n}{\lambda_n} (1 - e^{-\lambda_n t}) \frac{\sin\sqrt{\frac{\lambda_n - k}{D}} h_0^2}{\sqrt{\frac{\lambda_n - k}{D}} h_0^2} \sin\sqrt{\frac{\lambda_n}{D_{\text{wax}}}} h_{\text{wax}}^2 \right] \quad (13)$$

The resistance of the Mg film is related to its thickness by $R/R_0 = h_0/h$, where R_0 is the initial resistance. The critical time t_c it takes for the resistance to double ($R = 2R_0$) is then determined by $h(t_c)/h_0 = 0.5$. Here, the material parameter including $M_{H_2O} = 18 \text{ g mol}^{-1}$, $M_{Mg} = 24 \text{ g mol}^{-1}$, $\rho_{Mg} = 1.738 \text{ g cm}^{-3}$, $w_0 = 1 \text{ g cm}^{-3}$, $k = 1.2 \times 10^{-3} \text{ s}^{-1}$ and $D = 6.0 \times 10^{-16} \text{ m}^2 \text{ s}^{-1}$ are from Li et al.,^[42] except for the water diffusivity in wax D_{wax} , which is obtained by fitting the experimental data as $D_{wax} = 6.05 \times 10^{-15} \text{ m}^2 \text{ s}^{-1}$, as shown in Figure 1D.

In Vivo Degradation: Animal studies were performed in accordance with the National Institutes of Health Guide for the Care and Use of Laboratory Animals under experimental protocols approved by the Animal Studies Committee at Washington University in St. Louis. Animals were housed in a central animal care facility and given access to standard rodent chow and water ad libitum.

Anesthesia was induced and maintained by means of isoflurane gas (4%–2%, inhaled). The rat skin was shaved and sterilized. A small skin incision about 1 cm was made. From the incision, a small subcutaneous pocket was formed by dull dissection to embed the candelilla wax. After the implantation, skin incisions were closed with 4–0 nylon suture. Postoperatively, all animals were evaluated daily for clinical signs of distress and infection. Three months postoperatively was defined as the end time point.

Preparation of Conductive Wax Composites: Mechanical mixing of tungsten powder (C10, Buffalo Tungsten) with candelilla wax at 100 °C on a hotplate yielded well-dispersed mixtures. Melting and drop casting C-wax formed in this manner on a glass slide through a stencil mask produced well-defined patterns, including circles with diameters of 3 cm and line shapes with 0.5 cm widths and 2.5 cm lengths, for measurements of sheet resistance and tests of reliability (temperature dependence and water degradation), respectively.

In-Vitro Electrical Tests of Conductive Wax: Sheet resistances of C-wax with different loading fractions of W and candelilla wax were measured using a four-point probing tool (Jandel RM43 AR). With thicknesses determined by the caliper, these data yielded the conductivities of the samples. Placing a test structure of C-wax (line shape with 0.5 cm width, 2.5 cm length, and 0.1 mm thickness) on a hot plate allowed measurement of the resistance (FLUKE 87 multimeter) as a function of temperature. Each data point corresponds to a measurement at a given set temperature, stabilized for 10 min. Evaluations of the degradation of C-wax in water involved submerging samples in PBS solution. A thermometer placed next to the samples enabled temperature readings. The resistance values were averaged from five different samples for each test.

Fabrication of Mg-Based Wireless Circuit on Wax Substrate: A glass slide coated with a thin film of PDMS served as a temporary substrate for a magnesium foil ($\approx 50 \text{ }\mu\text{m}$, Solution Materials, LLC, USA). Glass slides were pre-cleaned in a mixture of acetic acid and DI water (1:10). Photolithography and wet etching in diluted hydrochloric acid (HCl:DI water = 1:9) defines RF coil structures from the foil. A physical transfer process delivers the Mg RF coil onto the surface of a PLGA substrate. The Mg RF coil/PLGA structure was then laminated on a substrate of candelilla wax. Dip coating in molten candelilla wax forms the encapsulation layer.

Differential Scanning Calorimetry (DSC): Thermal analysis was performed with a TA Instruments Q100 DSC unit. The temperature program involved a ramp of $10 \text{ }^\circ\text{C min}^{-1}$ from $0 \text{ }^\circ\text{C}$ and $100 \text{ }^\circ\text{C}$. To avoid hysteresis, data were recorded only during the second heating cycle. Test samples had weights between 20 and 25 mg, and were sealed in an aluminum hermetic pan prior to thermal analysis.

Biocompatibility Studies: All experiments were performed in accordance with the National Institute of Health guidelines and received the approval of the Animal Care and Use Committee of Washington University School of Medicine. Adult C57/B6 male mice were 8–12 weeks of age at the beginning of the study. All mice were housed in the animal facilities of the Washington University School of Medicine on a 12 h light/dark cycle, with ad libitum access to food and water. Wax samples ($1 \text{ cm} \times 1 \text{ cm} \times 800 \text{ }\mu\text{m}$) were implanted subcutaneously in the abdominal region. Skin tissue samples were collected from mice either 1 or 2 months after implantation, or sham surgery ($n = 2\text{--}3$ for each

group). Sham surgery was performed as an incision, but no placement of wax. Weights of mice were recorded at each time point baseline, 1 and 2 months. For collection of skin samples, mice were perfused with 4% paraformaldehyde (PFA), as previously described, and skin directly in contact with wax (or incision point, for sham), was harvested.^[43] Samples were post-fixed in 4% PFA overnight, transferred to 30% sucrose solution for 24 h, frozen down in O.C.T. Compound (Tissue-Tek, 4583) and sectioned on a cryostat (Leica) at $20 \times 10^{-6} \text{ m}$ onto slides. For staining, slides were post-fixed with 4% PFA for 5 min, thoroughly washed in $1\times$ PBS, and then submerged in sodium citrate buffer ($10 \times 10^{-3} \text{ M}$ Sodium Citrate, 0.05% Tween 20, pH 6.0; @ $95\text{--}100 \text{ }^\circ\text{C}$) for 20 min. The slides were allowed to cool in the buffer solution for an additional 20 min, washed in $1\times$ PBS and incubated in blocking solution (5% normal goat serum/0.3% Triton-X in $1\times$ PBS) for 1 h at RT. Slides were incubated in primary antibody (1:500 Mouse anti-CD45, BD Pharmingen; 550539, in blocking solution) overnight at $4 \text{ }^\circ\text{C}$, washed with $1\times$ PBS, and then incubated in secondary antibody (1:1000 Goat anti-rat IgG Alexa Fluor 488, Thermo Fischer; A11006, in blocking solution) for 45 min at RT. Lastly, slides were washed with $1\times$ PBS, and coverslipped (ProLong Gold antifade reagent, Molecular Probes; P36934). For H&E staining, slides were post-fixed in ethanol stained with a standard H&E protocol.^[43]

Slides were stained in two batches and imaged all at once. The same camera settings were used for all images and no changes were made to the images individually. CD45 immunofluorescence staining intensity was quantified using ImageJ (NIH). For quantification 8–6 images were taken from 2 to 4 bladder sections from each animal by an experimenter blinded to treatment group. Sections were separated by at least $100 \times 10^{-6} \text{ m}$. For intensity, images at threshold were applied to remove the bottom 50% of the signal and then the overall pixel intensity was quantified. Sub-cutaneous Complete Freund's Adjuvant (CFA, $10 \text{ }\mu\text{L}$) was injected 24 h prior to tissue harvesting to initiate an immune response, this tissue was used as a positive control for the CD45 staining.

Supporting Information

Supporting Information is available online from Wiley Inter Science or from the author.

Acknowledgements

S.M.W., J.K., and K.E.C. contributed equally to this work. This work was funded in part by the National Institutes of Health (NIH) Director's Transformative Research Award (NS081707), an award from National Institute of Biomedical Imaging and Bioengineering (EB021793) to R.W.G. and J.A.R., National Research Service Award (DK115122) awarded to A.D.M., and the T32 training grant (DA007261) to L.A.M. Y.H. acknowledges the support from National Science Foundation (Grant 1400169, 1534120, and 1635443) and NIH (Grant R01EB019337). Y.X. gratefully acknowledges support from the Ryan Fellowship and the Northwestern University International Institute for Nanotechnology.

Conflict of Interest

The authors declare no conflict of interest.

Keywords

bioresorbable electronics, bioresorbable polymers, conductive composites, encapsulation, wax

Received: March 12, 2018

Revised: May 15, 2018

Published online: June 25, 2018

- [1] K. N. Burns, K. Sun, J. N. Fobil, R. L. Neitzel, *Int. J. Environ. Res. Public Health* **2016**, *13*, 140.
- [2] M. Heacock, C. B. Kelly, K. A. Asante, L. S. Bimbaum, Å. L. Bergman, M. N. Bruné, I. Buka, D. O. Carpenter, A. Chen, X. Huo, M. Kamel, P. J. Landrigan, F. Magalini, F. Diaz-Barriga, M. Neira, M. Omar, A. Pascale, M. Ruchirawat, L. Sly, P. D. Sly, M. V. Berg, W. A. Suk, *Environ. Health Perspect.* **2016**, *124*, 550.
- [3] K. K. Fu, Z. Wang, J. Dai, M. Carter, L. Hu, *Chem. Mater.* **2016**, *28*, 3527.
- [4] X. Huang, Y. Liu, S. W. Hwang, S. K. Kang, D. Patnaik, J. F. Cortes, J. A. Rogers, *Adv. Mater.* **2014**, *26*, 7371.
- [5] Y. H. Jung, T. H. Chang, H. Zhang, C. Yao, Q. Zheng, V. W. Yang, H. Mi, M. Kim, S. J. Cho, D. W. Park, H. Jiang, J. Lee, Y. Qiu, W. Zhou, Z. Cai, S. Gong, Z. Ma, *Nat. Commun.* **2015**, *6*, 7170.
- [6] M. Irimia-Vladu, P. A. Troshin, M. Reisinger, L. Shmygleva, Y. Kanbur, G. Schwabegger, M. Bodea, R. Schwödauier, A. Mumyatov, J. W. Fergus, V. F. Razumov, H. Sitter, N. S. Saricifci, S. Bauer, *Adv. Funct. Mater.* **2010**, *20*, 4069.
- [7] X. Jia, C. Wang, C. Zhao, Y. Ge, G. G. Wallace, *Adv. Funct. Mater.* **2016**, *26*, 1454.
- [8] K. J. Yu, D. Kuzum, S. W. Hwang, B. H. Kim, H. Juul, N. H. Kim, S. M. Won, K. Chiang, M. Trumpis, A. G. Richardson, H. Cheng, H. Fang, M. Thompson, H. Bink, D. Talos, K. J. Seo, H. N. Lee, S. K. Kang, J. H. Kim, J. Y. Lee, Y. Huang, F. E. Jensen, M. A. Dichter, T. H. Lucas, J. Viventi, B. Litt, J. A. Rogers, *Nat. Mater.* **2016**, *15*, 782.
- [9] S. K. Kang, R. K. J. Murphy, S. W. Hwang, S. M. Lee, D. V. Harburg, N. A. Krueger, J. Shin, P. Gamble, H. Cheng, S. Yu, Z. Liu, J. G. McCall, M. Stephen, H. Ying, J. Kim, G. Park, R. C. Webb, C. H. Lee, S. Chung, D. S. Wie, A. D. Gujar, B. Vemulapalli, A. H. Kim, K. M. Lee, J. Cheng, Y. Huang, S. H. Lee, P. V. Braun, W. Z. Ray, J. A. Rogers, *Nature* **2015**, *530*, 71.
- [10] C. H. Lee, H. Kim, D. V. Harburg, G. Park, Y. Ma, T. Pan, J. S. Kim, N. Y. Lee, B. H. Kim, K. I. Jang, S. K. Kang, Y. Huang, J. Kim, K. M. Lee, C. Leal, J. A. Rogers, *NPG Asia Mater.* **2015**, *7*, e227.
- [11] H. Tao, S.-W. Hwang, B. Marelli, B. An, J. E. Moreau, M. Yang, M. A. Brenckle, S. Kim, D. L. Kaplan, J. A. Rogers, F. G. Omenetto, *Proc. Natl. Acad. Sci. USA* **2014**, *111*, 17385.
- [12] S. W. Hwang, H. Tao, D. H. Kim, H. Cheng, J. K. Song, E. Rill, M. A. Brenckle, B. Panilaitis, S. M. Won, Y. S. Kim, Y. M. Song, K. J. Yu, A. Ameen, R. Li, Y. Su, M. Yang, D. L. Kaplan, M. R. Zakin, M. J. Slepian, Y. Huang, F. G. Omenetto, J. A. Rogers, *Science* **2012**, *337*, 1640.
- [13] S. W. Hwang, D. H. Kim, H. Tao, T. I. Kim, S. Kim, K. J. Yu, B. Panilaitis, J. W. Jeong, J. k. Song, F. G. Omenetto, J. A. Rogers, *Adv. Funct. Mater.* **2013**, *23*, 4087.
- [14] S. W. Hwang, G. Park, C. Edwards, E. A. Corbin, S. K. Kang, H. Cheng, J. K. Song, J. H. Kim, S. Yu, J. Ng, J. E. Lee, J. Kim, C. Yee, B. Bhaduri, Y. Su, F. G. Omenetto, Y. Huang, R. Bashir, L. Goddard, G. Popescu, K. M. Lee, J. A. Rogers, *ACS Nano* **2014**, *8*, 5843.
- [15] L. Yin, A. B. Farimani, K. Min, N. Vishal, J. Lam, Y. K. Lee, N. R. Aluru, J. A. Rogers, *Adv. Mater.* **2015**, *27*, 1857.
- [16] S. K. Kang, G. Park, K. Kim, S. W. Hwang, H. Cheng, J. Shin, S. Chung, M. Kim, L. Yin, J. C. Lee, K. M. Lee, J. A. Rogers, *ACS Appl. Mater. Interfaces* **2015**, *7*, 9297.
- [17] S. W. Hwang, X. Huang, J. H. Seo, J. K. Song, S. Kim, S. Hage-Ali, H. J. Chung, H. Tao, F. G. Omenetto, Z. Ma, J. A. Rogers, *Adv. Mater.* **2013**, *25*, 3526.
- [18] L. Yin, H. Cheng, S. Mao, R. Haasch, Y. Liu, X. Xie, S. W. Hwang, H. Jain, S. K. Kang, Y. Su, R. Li, Y. Huang, J. A. Rogers, *Adv. Funct. Mater.* **2014**, *24*, 645.
- [19] C. J. Bettinger, Z. Bao, *Adv. Mater.* **2010**, *2*, 651.
- [20] S. K. Kang, S. W. Hwang, H. Cheng, S. Yu, B. H. Kim, J. H. Kim, Y. Huang, J. A. Rogers, *Adv. Funct. Mater.* **2014**, *24*, 4427.
- [21] Y. K. Lee, K. J. Yu, Y. Kim, Y. Yoon, Z. Xie, E. Song, H. Luan, X. Feng, Y. Huang, J. A. Rogers, *ACS Appl. Mater. Interfaces* **2017**, *9*, 42633.
- [22] S. K. Kang, S. W. Hwang, S. Yu, J. H. Seo, E. A. Corbin, J. Shin, D. S. Wie, R. Bashir, Z. Ma, J. A. Rogers, *Adv. Funct. Mater.* **2015**, *25*, 1789.
- [23] A. E. V. Petersson, L. M. Gustafsson, M. Nordblad, P. Borjesson, B. Mattiasson, P. Adlercreutz, *Green Chem.* **2005**, *7*, 837
- [24] N. Gontard, S. Guilbert, *Food Packaging and Preservation*, Springer, Boston, **1994**, pp. 159–181.
- [25] R. N. Tharanathan, *Trends Food Sci. Technol.* **2003**, *14*, 71.
- [26] R. Rojas-Molina, M. A. De León-Zapata, S. Saucedo-Pompa, M. A. Aguilar-Gonzalez, C. N. Aguilar, *J. Med. Plants Res.* **2013**, *7*, 702.
- [27] H. C. Chen, C.-H. Kuo, H. H. Chen, Y.-C. Liu, C. J. Shieh, *J. Am. Oil Chem. Soc.* **2011**, *88*, 1917
- [28] A. Asperger, W. Engewald, G. Fabian, *J. Anal. App. Pyrol.* **2001**, *61*, 91.
- [29] M. Regert, J. Langlois, S. Colinart, *J. Chrom. A.* **2005**, *1091*, 124.
- [30] U. Wolfmeier, H. Schmidt, F. Heinrichs, G. Michalczyk, W. Payer, W. Dietsche, K. Boehlke, G. Hohner, J. Wildgruber, *Ullmann's Encyclopedia Ind. Chem.* **2000**, *39*, 112.
- [31] S. F. Sabato, B. Ouattara, H. Yu, G. D'Aprano, C. Le Tien, M. A. Mateescu, M. Lacroix, *J. Agric. Food Chem.* **2001**, *49*, 1387.
- [32] E. A. Veraverbeke, P. Verboven, N. Scheerlinck, M. L. Hoang, B. M. Nicolai, *J. Food Eng.* **2003**, *58*, 285.
- [33] Y. M. Pogosyan, T. V. Khanamiryan, A. Y. Pogosyan, E. K. Avetisyan, S. S. Burnazyan, *Balkan J. Stomatol.* **2011**, *15*, 142.
- [34] E. P. Mamunya, V. V. Davidenko, E. V. Lebedev, *Polym. Compos.* **1995**, *16*, 319.
- [35] G. R. Fischer, S. Yoshikawa, R. E. Newnham, *J. Appl. Phys.* **1992**, *72*, 953.
- [36] S. Lee, J. Koo, S.-K. Kang, G. Park, Y. J. Lee, Y.-Y. Chen, S. A. Lim, K.-M. Lee, J. A. Rogers, *Mater. Today* **2018**, *21*, 207.
- [37] K. Zhang, B. Han, X. Yu, *Energy Convers. Manag.* **2012**, *64*, 62.
- [38] N. Ukrainczyk, S. Kurajica, J. Šipušić, *Chem. Biochem. Eng.* **2010**, *24*, 129.
- [39] M. Peuster, C. Fink, P. Wohlsein, M. Bruegmann, A. Günther, V. Kaese, M. Niemeyer, H. Haferkamp, C. von Schnakenburg, *Bio-materials* **2003**, *24*, 393.
- [40] M. Peuster, C. Fink, C. von Schnakenburg, *Biometaterials* **2003**, *24*, 4057.
- [41] S. Kanokpanont, S. Damrongsakkul, J. Ratanavaraporn, P. Aramwit, *Int. J. Biol. Macromol.* **2013**, *55*, 88.
- [42] R. Li, H. Cheng, Y. Su, S.-W. Hwang, L. Yin, H. Tao, M. A. Brenckle, D.-H. Kim, F. G. Omenetto, J. A. Rogers, Y. Huang, *Adv. Funct. Mater.* **2013**, *23*, 3106.
- [43] S. I. Park, D. S. Brenner, G. Shin, C. D. Morgan, B. A. Copits, H. U. Chung, M. Y. Pullen, K. N. Noh, S. Davidson, S. J. Oh, J. Yoon, K. I. Jang, V. K. Samineni, M. Norman, J. G. Grajales-Reyes, S. K. Vogt, S. S. Sundaram, K. M. Wilson, J. S. Ha, R. Xu, T. Pan, T. I. Kim, Y. Huang, M. C. Montana, J. P. Golden, M. R. Bruchas, R. W. Gereau, J. A. Rogers, *Nat. Biotechnol.* **2015**, *33*, 1280.